deforming high-molecular-weight glassy polymer at 386 K is nearly identical to the penetration rate at the glass transition temperature of 486 K. Without active plastic flow, the penetration rate at 386 K is immeasurable, which indicates that the observed effect of plastic flow in this glass is equivalent to an increase in the diffusion constant by as much as a factor of 2×10^4 (27). Corresponding experiments in amorphous metals have not yet been performed, and there are important topological differences between glassy polymers and glassy metal alloys. However, there exists a striking similarity in the phenomenology and deformation mechanisms between the metallic and polymeric glasses (28). Therefore, we conclude that the observed rapid formation of Zr_2Ni nanocrystallites around the shear bands of our bulk amorphous alloy is a direct consequence of the inevitable dynamic flow dilatation in the actively deforming bands (without any substantial increase in temperature during plastic flow) and of the attendant dramatic enhancement in atomic diffusional mobility.

The present work provides direct experimental evidence that controlled and highly confined local contact deformation in the form of quasi-static nanoindentation of a bulk metallic glass at room temperature results in nanocrystallization. Additional features of the present experiments are that nanocrystallization due to ultrafine-scale contact occurs even without the possibility of substantial local heating and that the nanocrystallites are identified to be the same as those found during thermal anneal at 783 K without

any mechanical deformation or indentation. To explain these results, we invoke a mechanistic rationale predicated on radically enhanced atomic diffusional mobility by drawing an analogy with recent experimental observations of enhanced diffusion in actively deforming amorphous polymers.

References and Notes

1. Y. He, S. J. Poon, G. J. Shiflet, *Science* **241**, 1640 (1988).
2. A. L. Greer, *Science* **267**, 1947 (1995).
3. I. Mat'ko, E. Illeková, P. Švec, P. Duhaj, *Mater. Sci. Eng.* **A225**, 145 (1997).
4. A. Makino, A. Inoue, T. Masumoto, *Mater. Trans. Jpn. Inst. Mater.* **36**, 924 (1995).
5. T. Masumoto, R. Maddin, *Mater. Sci. Eng.* **19**, 1 (1975).
6. H. Chen, Y. He, G. J. Shiflet, S. J. Poon, *Nature* **367**, 541 (1994).
7. A. Inoue, T. Zhang, T. Masumoto, *Mater. Trans. Jpn. Inst. Mater.* **31**, 177 (1990).
8. A. Peker, W. L. Johnson, *Appl. Phys. Lett.* **63**, 2342 (1993).
9. S. Suresh, Ed., *Acta Mater.* **48** (The Millennium Special Issue), 279 (2000).
10. P. E. Donovan, *Acta Metall.* **37**, 445 (1989).
11. J. G. Wang, B. W. Choi, T. G. Nieh, C. T. Liu, *J. Mater. Res.* **15**, 798 (2000).
12. R. Vaidyanathan, M. Dao, G. Ravichandran, S. Suresh, *Acta Mater.* **49**, 3781 (2001).
13. W. J. Wright, R. Saha, W. D. Nix, *Mater. Trans. Jpn. Inst. Mater.* **42**, 642 (2001).
14. Y. He, G. J. Shiflet, S. J. Poon, *Acta Metall. Mater.* **43**, 83 (1995).
15. K. Lu, *Mater. Sci. Eng.* **R16**, 161 (1996).
16. C. T. Liu *et al.*, *Metall. Mater. Trans. A* **29A**, 1811 (1998).
17. Nanoindentation experiments were conducted in a load-control mode with a NanoTest 600 (MicroMaterials, Wrentham, UK). For TEM observation, up to 400 indentations, equally spaced in the horizontal and the vertical directions with 20-μm separation, were made on the specimen that was previously cut into a disk 3 mm in diameter. For AFM, 10 indents for each load level were made. Electron microscopy studies were made using model 200CX, JEOL TEM (JEOL, Tokyo, Japan) operating at 200 kV. We prepared the specimens for TEM observations by ion-milling methods using a Gatan Duo-Mill (Gatan, Warrendale, PA) at 0.5 mA and 4 kV. The AFM studies were conducted on Nanoscope IIIa Scanning Probe Microscope from Digital Instruments.
18. B. Cantor, in *Amorphous Metals and Semiconductors*, P. Haasen, R. I. Jaffee, Eds. (Pergamon, Oxford, UK, 1986), pp. 108–125.
19. H. J. Leamy, H. S. Chen, T. T. Wang, *Metall. Trans.* **3**, 699 (1972).
20. J. D. Eshelby, P. L. Pratt, *Acta Metall.* **4**, 560 (1956).
21. H. Neuhauser, *Scr. Metall.* **12**, 471 (1978).
22. A. S. Argon, *Acta Metall.* **27**, 47 (1979).
23. K. M. Flores, R. H. Dauskardt, *J. Mater. Res.* **14**, 638 (1999).
24. W. H. Wang, D. W. He, D. Q. Zhao, T. S. Yao, M. He, *Appl. Phys. Lett.* **75**, 2770 (1999).
25. F. Spaepen, *Acta Metall.* **25**, 407 (1977).
26. J. Megusar, A. S. Argon, N. J. Grant, in *Rapidly Solidified Amorphous and Crystalline Solids*, B. H. Kear, B. C. Giessen, M. Cohen, Eds. (Elsevier, Amsterdam, Netherlands, 1982), pp. 283–287.
27. Q.-Y. Zhou, A. S. Argon, R. E. Cohen, *Polymer* **42**, 613 (2001).
28. A. S. Argon, in *Materials Science and Technology*, R. W. Cahn, P. Haasen, E. J. Kramer, Eds. (VCH, Weinheim, Germany, 1993), vol. 6, pp. 461–508.
29. Supported by the Defense University Research Initiative on NanoTechnology (DURINT) on "Damage- and Failure-Resistant Nanostructured and Interfacial Materials," funded at the Massachusetts Institute of Technology by the Office of Naval Research under grant N00014-01-1-0808. The authors are grateful to K. J. Van Vliet for valuable assistance with nanoindentation experiments, R. Vaidyanathan for helpful discussion, and C. T. Liu for providing the specimens. J.J.K. is grateful to the Center for Advanced Aerospace Materials at POSTECH, Pohang, Republic of Korea, for a postdoctoral fellowship.
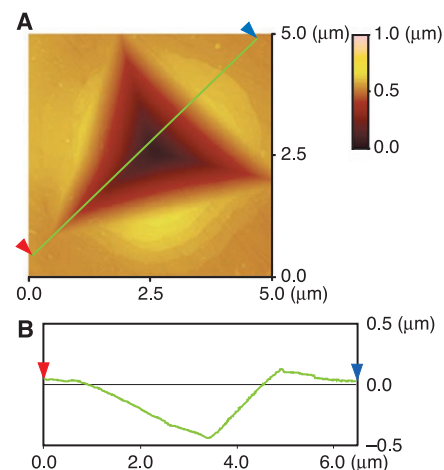
Fig. 3. AFM analysis after 60 mN of maximum load. (**A**) AFM height mode image (5 μm by 5 μm) of an indent. We also see the characteristic circular patterns around such an indent again, and the colored height information around the triangular indent reveals both large material pileup at the perimeter of the indent and overlapping layers of severely displaced materials. (**B**) Cross-sectional profile of the indent, along the green line of (A), showing the surface uplift along one side to be as high as 150 nm above the reference surface. This large pileup height around the perimeter of the indent, compared to the penetration depth (720 nm), indicates the severity of plastic flow around this region during indentation.

Mineral Surface Control of Organic Carbon in Black Shale

Martin J. Kennedy,[1]* David R. Pevear,[1] Ronald J. Hill[2]

We show that 85% of variation in total organic carbon can be explained by mineral surface area in a black shale deposit from two locations in the late Cretaceous Western Interior Seaway, United States. This relation suggests that, as in modern marine sediments, adsorption of carbon compounds onto clay mineral surfaces played a fundamental role in the burial and preservation of organic carbon. Our data also provide evidence for organic matter within the smectite interlayer. This association implies that organic carbon sequestration in a representative oil-prone black shale facies may be more closely related to patterns of continental weathering and clay mineralogy than to ocean water chemistry or marine productivity.

The stratigraphic record is punctuated by intervals of organic carbon-rich sediments that form laterally persistent black marine shale and mudrock (1, 2). Many of these are important petroleum sources. It has been generally thought that organic matter (OM) in shale was deposited as discrete biogenic materials or particles, and the presence of these in shales has also been used to infer periods of ocean anoxia. Here we present evidence for an alternative model for the genesis of black shales, in which detrital smectite or smectitic mixed-layer illite-smectite (I-S)

[1]Department of Earth Science, University of California, Riverside, CA 92521, USA. [2]U.S. Geological Survey, Box 25045, Denver Federal Center, Mail Stop 939, Denver, CO 80225, USA.

*To whom correspondence should be addressed. E-mail: martink@mail.ucr

clays facilitate OM burial (Fig. 1). Smectitic clays have a large reactive surface capable of sorbing meaningful amounts of dissolved organic compounds from seawater or pore fluids, and they can also act as a preservative during burial.

In modern continental margin sediments, discrete particulate OM constitutes a minor portion (<10%) of total organic carbon (TOC), with the dominant portion being sorbed or otherwise associated with mineral surfaces (3–6). TOC in these sediments is related to the external surface area of minerals, such that OM covers mineral surfaces uniformly (but not necessarily completely) (3, 4, 6). Mineral surfaces help to preserve OM through deposition, burial, and lithification (4, 7, 8). Together, these findings imply that carbon burial in modern continental margin settings may be strongly influenced by the available mineral surface area (MSA), which is in turn a function of the abundance and mineralogy of weathering-derived clay minerals (9). We propose that abundant MSA was a necessary starting condition for the burial and preservation of OM in certain black shales, and that the bulk of the OM is molecular-scale adsorbed and not particulate (as in conventional models). MSA is thus the first-order control on the burial and preservation of OM in these ancient organic-rich deposits, with conventional paleoceanographic controls constituting a second-order or modifying effect.

To test whether there is a positive relation between MSA and TOC in black shales, we sampled an organic-poor to organic-rich (0.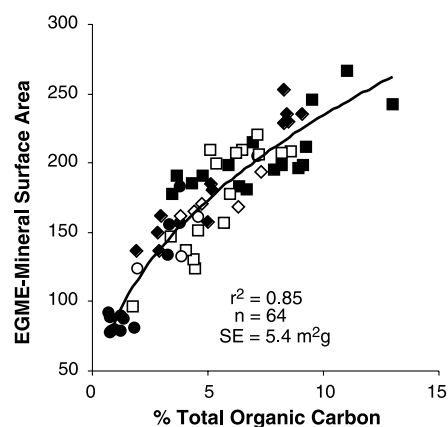5 to 13% TOC) interval through the Cretaceous (Campanian) upper Niobrara Formation and lower Pierre Shale and analyzed the stratigraphic trends in TOC, MSA, elemental composition, and clay mineralogy in Wyoming and South Dakota, USA (Fig. 2). These units are representative of well-studied late Cretaceous cyclical black shales (10). The presence of organic-rich facies has been suggested to imply ocean stratification and anoxia (11), upwelling-induced high productivity (12), or changes in dilution and winnowing of the nonorganic fraction (13). The lower Pierre Shale shows a broad range of TOC, allowing comparison of TOC stratigraphic trends with MSA and paleoenvironmental variation to determine the dominant influences on OM burial. The units studied have not undergone sufficient burial to result in diagenetic alteration of detrital clay minerals (10) or thermal maturation of organic carbon (11). The (minor) contribution of smectite from in situ alteration of volcanic ash was resolved using the differences in Zr concentration in bentonite (260 ppm) relative to the global average for black shale (170 ppm) (Fig. 2F).

The upper Niobrara Formation and lower Pierre Shale constitute an interval of finely laminated, dark-colored mudrock composed of clay minerals (60 to 70%), quartz (20 to 30%), and minor feldspar and carbonate (<5%). An abundance of I-S reflects weathering of volcanic rocks in the Sevier Province to the northwest, whereas kaolinite and chlorite are from cratonic sources to the west and east (10). Organic matter is dominantly amorphous, type II marine (11). Undisturbed lamination, a depauperate benthic community, and the sulfur chemistry are consistent with recurrent anoxic-dysoxic conditions during deposition (11) at ∼200 m water depth (10, 12, 13).

Thin section petrography shows minor lithological or grain size variation across the profile, and evidence of current reworking is rare. Subtle variations occur in samples coinciding with the interpreted condensed interval at level A, where there is an increase in fecal pellets, fish scales, apatite, radiolarians, and pyrite. Structured particulate OM is sparse [in keeping with (10)]. Discontinuous stringers of structureless (amorphous) OM enveloping clay minerals are present in high-TOC (>8%) intervals. Although we recognize a conventional interpretation that "amorphous OM" is of particulate (particularly algal) origin, we feel strongly that there is no direct evidence to substantiate this in our samples. The amorphous component (visible in kerogen concentrates after the silicate phase is dissolved) could equally be the product of adsorbed or mineral-associated OM.

Subtle changes in the depositional conditions of the lower Pierre Shale include variations in sedimentation rate, clay provenance, and weathering. At horizon A (Fig. 2), slow sedimentation rate (likely coinciding with the Clagett Transgression) is indicated by a condensed section with high frequency of bentonites, low TiO_2, high Si/Al ratio, and a quartz maximum [aeolian and biogenic origin (14)]. Above horizon A, clay mineral abundance increases (relative to quartz) to a maximum immediately below horizon B along with the proportion of smectite in the I-S component, and there is a decrease in the kaolinite + chlorite component of the <2 μm fraction. A parallel rise in the Mg/K ratio in the bulk sample (15) supports the x-ray data because smectite is Mg-rich, whereas illite is K-rich.

These trends suggest a shift from the relative importance of aeolian deposition of volcanic ash and quartz during transgression and sediment starvation (horizon A) to detrital clay contributed from increased continental
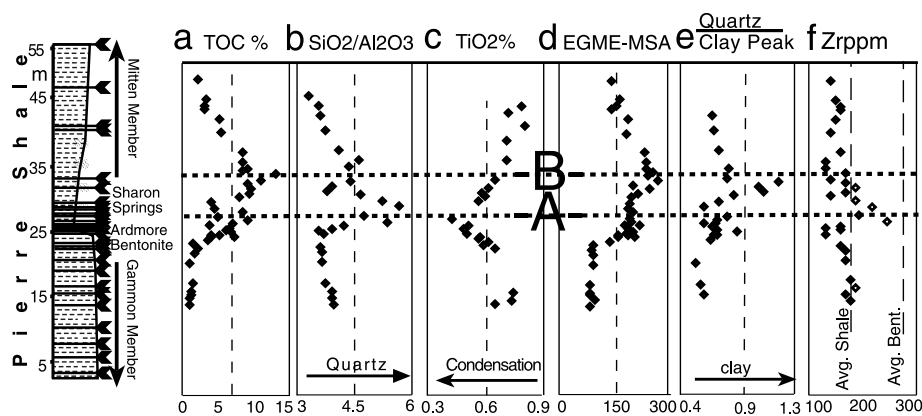

Fig. 1. Relation between EGME-MSA and TOC for lower Campanian to upper Campanian Niobrara Formation: gammon shale (circles), lower-upper Campanian Sharon Springs member of the Pierre Shale (squares), and upper Campanian mitten black shale member of the Pierre Shale (diamonds) (15). Two sections are shown: Red Bird, Wyoming (open symbols) and Oral, South Dakota (solid symbols), localities 16 and 18 of (10). Standard error of fit to modeled power function is 5.4 m^2g^{-1} for EGME with TOC as independent variable.

Fig. 2. Geochemical profiles [methods and data in (15)] of the Pierre Shale: (**a**) TOC; (**b**) SiO_2/Al_2O_3 (ratio of percentages), showing a maximum at horizon A likely corresponding to a decline in Al-rich detrital clay minerals (kaolinite) and an increase in aeolian quartz or biogenic silica; (**c**) TiO_2 minima, providing further evidence for condensation at horizon A implying a decline in detrital minerals, including silt-sized titanomagnetite, rutile, and sphene; (**d**) EGME-MSA for samples untreated with H_2O_2; (**e**) relative clay mineral versus quartz peak areas by XRD (clay minerals reach a maximum toward horizon B); (**f**) Zr used as an index of diagenetic smectite contribution from Zr-rich bentonite with global and average bentonite values from (10).

runoff (horizon B). We measured MSA using a conventional EGME method [ethylene glycol monoethyl ether (*15, 16*)] as well as the external surface area measured by N_2 adsorption [Brunauer-Emmett-Teller (BET) adsorption isotherm] (Fig. 3B) (*15*) to determine the role of interlayer sites in OM preservation. Because smectite has appreciably more surface area ($800\ m^2\ g^{-1}$ external and interlayer) than does illite ($30\ m^2\ g^{-1}$), kaolinite, chlorite, or quartz ($<20\ m^2\ g^{-1}$) (*9*), the peak in EGME-MSA at horizon B reflects an increase in smectitic clay minerals, not simply the total percent clay. This shift is most likely driven by a change in provenance or weathering intensity.

The maximum in TOC coincides with the peak in EGME-MSA (horizon B) and also covaries with this parameter through the section (Fig. 1). It does not coincide with a time of low sedimentation rate (horizon A) nor with an oscillating signal; this finding argues against reduced clastic dilution or recurring oxic-dysoxic cycles as the dominant control on TOC. Fine grain size might reduce exposure to oxygen, thus preserving OM, but we do not see size variations that could explain a 12% range in TOC. The minor size variation, with prolonged exposure to oxidants in a distal setting with slow sedimentation rates (<10 cm per 1000 years), would argue that time, not grain size, could be more important in controlling oxidant exposure time, and the very intervals we see enriched should be the most lean. Selective hydrodynamic sorting could concentrate fine-grained OM with clays, but this does not explain the shift to high-MSA (I-S) clays that determine this re-

lation. Further, petrography shows a pelagic source with little winnowing or sorting.

This comparison suggests a linkage between TOC and EGME-MSA, and, by extrapolation, a linkage to the control of EGME-MSA by detrital smectite. The relation between smectite x-ray diffraction (XRD) peak intensities ($<2\ \mu m$ fraction) and TOC (Fig. 3C) is strong for samples with a limited contribution of diagenetic smectite from volcanic ash [samples with <180 ppm Zr (*15*)]. The four samples with anomalous Zr plot off this trend, reinforcing the interpretation that the OM and mineral surfaces become associated in the depositional environment and not in the burial diagenetic environment, where volcanic glass has altered to smectite.

The relation (Fig. 1) of TOC with EGME-MSA extends well past known BET-MSA values (BET for smectite $<50\ m^2\ g^{-1}$ reflecting only the external MSA), which show no relation with TOC (Fig. 3B). This finding implies that OM is present dominantly within smectite interlayer sites. Many types of polar or charged molecules enter interlayer sites from aqueous solution (*17, 18*), including atrazine (*19*), humic acid (*20, 21*), and proteins (*22, 23*). The last two groups are readily available in soil and marine environments (*24, 25*). Although neutral or nonpolar molecules may be unlikely to enter pristine interlayer sites from aqueous solution, small loadings of sorbed polar molecules open the interlayer and make it more hydrophobic so that neutral molecules are easily sorbed (*18*). Interlayer OM may also form by coalescence of thin OM-coated smectite crystals in the

shallow burial environment, converting initial external surface into interlayer surface [i.e., the quasi-crystal model of (*19*)]. More recently, the sorption of organic compounds within the interlayer space of smectite has been attributed to multiple mechanisms involving siloxane surfaces as well as water and interlayer cations (*17*). The role of interlayer spaces of smectite in sequestering OM is accepted in the soil science community, and there is every reason to believe that this same mechanism may play a role in burial and preservation of OM in marine sediments as well.

The internal (interlayer) surface of smectite, unique among marine clay minerals, may also explain the logarithmic shape of Fig. 1. As total MSA increases, the relative amount (from XRD) of smectite as a percentage of total clay minerals also increases. Therefore, there would appear to be more TOC associated with a unit of smectite surface than with a similar unit of kaolinite or chlorite surface. Either the interlayer surface of smectite can sustain an initially higher loading of OM, or it protects OM from subsequent metabolization or oxidation more efficiently than does the external surface. An association of smectite with high TOC has also been reported in modern marine sediments (*26, 27*).

Our data show that mineral surface adsorption of dissolved organic compounds offers an alternative mechanism for carbon preservation and burial in the geologic past. Its role in black shale formation is reasonable because of its demonstrated importance in modern sediments. Our initial investigation of black shales shows a strong relation between MSA and TOC, implying that MSA provides a first-order control on organic carbon burial. The strength of this relation extends across a broad range of TOC and MSA values, which suggests that interlayer sites within I-S clays may take up and preserve OM, and that external surface area (conventional BET) may not adequately characterize the system in smectitic sediments.

This hypothesis provides a unifying principle linking inorganic and organic processes (e.g., it implies a mineral surface condensation model for the formation of amorphous kerogen). Further, the initial close association of mineral and organic compounds implies an oil-wet condition that sets the stage for subsequent mineral-influenced catalysis during catagenesis and oil generation. Our work provides a simple mechanistic model capable of explaining abrupt alternation between organic-rich and organic-lean couplets via high-frequency changes in terrigenous deposition and continental weathering. A corollary of this hypothesis is that organic carbon is derived from the relatively limitless pool of dissolved organic carbon in seawater and pore fluids, and that interlayer MSA and the
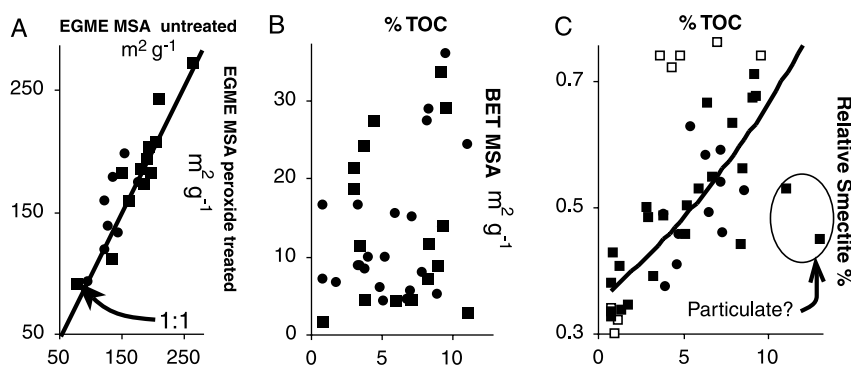

Fig. 3. Geochemical plots for both sections. (**A**) Samples treated with H_2O_2 to remove OM are statistically similar to untreated ones. This indicates that adsorption of EGME on OM is a minor contribution at best. Twenty samples were treated with 30% H_2O_2 (up to seven applications before reaction stopped) to oxidize organic material; <10% of original TOC was retained after H_2O_2 treatment (*n* = 11). Squares from Red Bird section; circles from Cheyenne River section. (**B**) BET external surface area plotted against TOC for samples treated with H_2O_2 to remove OM (squares) and untreated (circles). No relation is apparent, implying that OM is a function of internal surface area not measured by this technique. (**C**) Fraction of smectite relative to other clay minerals shows a relation with TOC for samples below 180 ppm Zr (solid squares from Cheyenne River section; solid circles from Red Bird section; open squares from the Cheyenne River section that contains >180 ppm Zr). High Zr indicates contribution to total MSA from diagenetic smectite that formed after the oceanic dissolved organic carbon reservoir was shut off from buried sediment. Samples with high TOC values that plot off the trend may indicate an additional source of carbon such as particulate organic material.

concentration of dissolved organic carbon ultimately limit organic carbon richness in marine sediments.

References and Notes

1. M. A. Arthur, B. B. Sageman, *Annu. Rev. Earth Planet. Sci.* **22**, 499 (1994).
2. P. B. Wignall, *Black Shales* (Clarendon, Oxford, 1994).
3. B. Ransom, R. H. Bennett, R. Baerwald, K. Shea, *Mar. Geol.* **138**, 1 (1997).
4. L. M. Mayer, *Geochim. Cosmochim. Acta* **58**, 1271 (1994).
5. A. N. Bishop, A. T. Kearsley, R. L. Patience, *Org. Geochem.* **18**, 431 (1992).
6. J. I. Hedges, R. G. Keil, *Mar. Chem.* **49**, 81 (1995).
7. R. G. Keil, J. I. Hedges, *Chem. Geol.* **107**, 385 (1993).
8. V. Salmon, S. Derenne, E. Lallier-Verges, C. Largeau, B. Beaudoin, *Org. Geochem.* **31**, 463 (2000).
9. E. Eslinger, D. Pevear, *Clay Minerals for Petroleum Geologists and Engineers, Short Course No. 22* (SEPM, Society for Sedimentary Geology, Tulsa, OK, 1988).
10. L. G. Schultz, H. A. Tourtelot, J. A. Gill, J. G. Boerngen,

Professional Paper 1064-B (U.S. Geological Survey, Washington, DC, 1980).
11. D. L. Gautier, J. L. Clayton, J. S. Lenethal, J. Reddin, *Hydrocarbon Source Rocks of the Greater Rocky Mountain Region*, J. Woodward, F. Meissner, J. L. Clayton, Eds. (Rocky Mountain Association of Geologists, Denver, 1984), pp. 369–385.
12. J. T. Parrish, D. L. Gautier, in *Evolution of the Western Interior Basin*, W. G. Caldwell, E. G. Kauffman, Eds. (Geological Association of Canada, Waterloo, Ontario, 1993), vol. 39, pp. 319–332.
13. G. S. Tanck, thesis, University of Arizona (1997).
14. W. E. Dean, M. A. Arthur, in *Stratigraphy and Paleoenvironment of the Cretaceous Western Interior Seaway, USA*, W. E. Dean, M. A. Arthur, Eds. (SEPM, Society for Sedimentary Geology, Tulsa, OK, 1998), vol. 6, pp. 227–255.
15. See supplemental data at *Science* Online (www.sciencemag.org/cgi/content/full/295/5555/657/DC1).
16. L. J. Cihacek, J. M. Bremer, *Soil Sci. Am. J.* **43**, 821 (1975).
17. G. Sheng, C. T. Johnston, B. J. Teppen, S. A. Boyd, *J. Agric. Food Chem.* **49**, 2899 (2001).

18. C. T. Johnston, in *Organic Pollutants in the Environment*, B. Sahwney, Ed. (Clay Minerals Society, Evergreen, CO 1996), vol. 8, pp. 1–44.
19. E. D. A. Barriuso, D. C. Laird, W. C. Koskinen, R. H. Dowdy, *Soil Sci. Am. J.* **58**, 1632 (1994).
20. H. Ohashi, H. Nakazawa, *Clay Miner.* **31**, 347 (1996).
21. M. Bosetto, P. Arfaioli, O. L. Pantani, G. G. Ristori, *Clay Miner.* **32**, 341 (1997).
22. P. Di Leo, *Clays Clay Miner.* **48**, 495 (2000).
23. A. A. Violante, M. A. De Cristofaro, M. A. Rao, L. Gianfreda, *Clay Miner.* **30**, 325 (1995).
24. J. I. Hedges, J. M. Oades, *Org. Geochem.* **27**, 319 (1997).
25. B. L. G. Theng, G. J. Churchman, R. H. Newman, *Soil Sci.* **142**, 262 (1986).
26. B. Ransom, K. Dongseon, M. Kastner, S. Wainwright, *Geochim. Cosmochim. Acta* **62**, 1329 (1998).
27. Y. Furukawa, *Org. Geochem.* **31**, 735 (2000).
28. S. J. Gregg, K. S. W. Sing, *Adsorption, Surface Area and Porosity* (Academic Press, London, ed. 2, 1982).
29. J. P. Quirk, S. Murray, *Soil Sci. Soc. Am. J.* **663**, 839 (1999).

Isolation and Structural Characterization of 1-Zirconacyclopent-3-yne, Five-Membered Cyclic Alkynes

Noriyuki Suzuki,* Masayoshi Nishiura, Yasuo Wakatsuki

Stable five-membered cyclic alkynes were synthesized, isolated, and fully characterized. Divalent zirconium species, bis(cyclopentadienyl)zirconium(II) equivalent, reacted with (*Z*)-1,4-disubstituted 1,2,3-butatrienes [(*Z*)-R-CH=C=C=CH-R, **1a**: R = (CH$_3$)$_3$Si-, **1b**: R = *tert*-C$_4$H$_9$-] to give 1-zirconacyclopent-3-yne compounds (**2a-b**) in good yields. X-ray diffraction analysis revealed their five-membered cyclic structure with a sufficiently short triple bond to regard this compound as a metallacyclopentyne.

Synthesis of small cyclic alkynes long has challenged organic chemists because of structural limitation (*1–3*). The C–C≡C–C moiety is normally linear, and cyclization creates highly strained and often labile species. Cyclopentynes, five-membered cyclic alkynes, have not been isolated yet because they are extremely reactive and unstable. Although several preparative methods of cyclopentynes have been reported (*4–6*), their existence was confirmed only spectroscopically in a matrix (*7*) or as trapped compounds by reactions such as [2+2] cycloaddition (*8*) or metal complexation (*9–11*). The resulting trapped compounds, however, no longer have C≡C triple bonds. The products of [2+2] cycloaddition are cyclopentene compounds. In the metal-coordinated cyclopentynes, the C≡C triple bond is elongated because of its coordination to the metal, and its length is in

a range of double bonds. 3,3,7,7-Tetramethylcycloheptyne, which contains a seven-membered ring, is the smallest hydrocarbyl cyclic alkyne isolated to date (*12*). Heterocyclic compounds that have longer heteroatomcarbon bonds are expected to give more stable cyclic alkynes. Indeed, silacycloheptynes are less reactive than hydrocarbyl analogs (*1, 13*). A silacyclic system even allowed isolation of a six-membered cyclic alkyne as 1,2,3,4-tetrasilacylohex-5-yne, although the ring contains four silicon atoms and only the triple bond consists of carbon atoms (*14*). With regard to a five-membered ring, the preparation of a thiacyclopentyne was reported (*15*). However, it was a short-lived species and isolation of a heterocyclic pentyne has not been successful. Organometallic compounds that contain metal-carbon bonds have allowed the isolation of small cyclic unsaturated compounds, such as metallacyclic cumulenes (*16, 17*). We reasoned that metallacyclic compounds may give stable small cyclic alkynes. We report here the synthesis and structural characterization of 1-zirconacyclopent-3-yne compounds that are stable and isolable and that can be fully characterized as five-membered cyclic alkynes.

Dichlorobis(cyclopentadienyl)zirconium (Cp$_2$ZrCl$_2$, Cp = η^5-C$_5$H$_5$) reacts with 2 equivalents of *n*-butyllithium or *n*-butyl Grignard reagent to form divalent zirconocene equivalent "Cp$_2$Zr" (Negishi reagent) (*18*). When we reacted this species with (*Z*)-1,4-bistrimethylsilyl-1,2,3-butatriene (**1a**) (*19*), 1-zirconacyclopent-3-yne (**2a**) was obtained in 89% yield after stirring at room temperature (rt) for 1 hour (Scheme 1) (*20*). Complex **2a** was an 83/17 mixture of cis and trans form at this stage. The cis-isomer gradually isomerized to trans at rt and gave a 36/64 mixture of *cis*/*trans*-**2a** that is in equilibrium after 48 hours. These compounds were very stable in solution at rt and were fully characterized by ^{1}H and ^{13}C nuclear magnetic resonance (NMR) spectroscopy. Two signals for the cyclopentadienyl (Cp) ligands were observed for the cis-isomers, whereas the Cp ligands are magnetically equivalent in the trans-isomers. A butatriene with *tert*-butyl groups, (*Z*)-2,2,7,7-tetramethyl-3,4,5-octatriene (**1b**) (*21*), also gave the zirconacyclopentyne **2b** after 1 hour at rt (yield 90% by ^{1}H NMR, cis/trans = 66/34), and the cis/trans ratio reached 12/88 after 48 hours.

These zirconacyclopentyne complexes **2a** and **2b** are so stable that the trans-isomers formed good crystals suitable for x-ray diffraction analysis. The molecular structure of *trans*-**2a** (Fig. 1) shows that the compound has a strained five-membered cyclic structure (*22*). The Zr atom and the four C atoms (C1-C4) in the cyclopentyne ring are coplanar.

Although there are several examples of butatriene complexes of transition metals (*23, 24*), no metallacyclopentyne complexes have been reported so far. In most of these complexes, a butatriene coordinates to the metal in η^2-fash-

RIKEN (The Institute of Physical and Chemical Research), Wako, Saitama 351-0198, Japan.

*To whom correspondence should be addressed. E-mail: nsuzuki@postman.riken.go.jp